MAGNETIC PROPERTIES OF AMORPHOUS IRON GERMANIUM FILMS

by

Ruthi Zielinski

AN UNDERGRADUATE THESIS

Presented to the Faculty of

The College of Arts and Sciences

At the University of Nebraska

For the Degree of Bachelor of Science

Major: Physics

Under the Supervision of
Prof. Dr. Robert Streubel and Prof. Dr. Shireen Adenwalla

Lincoln, Nebraska

March 2025

UNIVERSITY *of* NEBRASKA
LINCOLN

Contents

1 Abstract

The emergence of topological phases in condensed matter has traditionally been associated with symmetry (breaking) in long-range-ordered systems. Recent works on amorphous topological insulators, amorphous topological metals, amorphous superconductors, and amorphous topological magnetism demonstrated that this requirement of symmetry breaking also holds for disordered materials where larger exchange interactions and higher critical temperatures may arise. The underlying mechanisms of this emergent materials class are not yet understood. My thesis aims to elucidate the relationship between short-range order and magnetic properties of amorphous iron germanium films with different composition and thickness.

2 Introduction

2.1 Motivation

Amorphous materials are structurally disordered systems, characterized by a random (short-range-ordered) arrangement of atoms that lack an organized lattice structure and long-range order [1]. These materials typically have small magnetocrystalline anisotropy and magnetostriction as well as high resistivity and are normally soft-magnetic with a broad range of applications in electronics [2]. In the recent decades, there has been an increased interest in synthesis, structure, and properties of these materials. Our group's research efforts aim to help elucidate the extent to which structural disorder affects magnetic properties. Disordered material synthesis presents challenges as metals tend to form crystalline structures [3]. Our group uses molecular beam epitaxy, a form of physical vapor deposition [4], to create thin films. To create disordered materials, high cooling rates are required during vapor condensation to immobilize the atoms upon substrate contact, suppressing the atoms from repositioning to equilibrium lattice sites and crystallization [1, 5]. The fabrication of these materials is delicate as the resulting structure and magnetic properties of the thin films are extremely sensitive to composition variations and deposition conditions [6]. Thus, we take a holistic approach to varying compositions slightly as well as fabrication conditions to determine their effects on the thin film structure and respective magnetic properties. Fabrication conditions include factors, such as, deposition rates, rotation during deposition, stage used to hold substrate during deposition, the mounts holding the substrates as well as how the substrates are attached, etcetera.

The structural and chemical disorder in amorphous structures can create magnetically frustrated systems that possess degenerate ground states resulting from competing interactions with nearest and next-nearest neighbors. This infers the existence of multiple possible states with equal or similar energies [1]. The order-by-disorder phenomenon refers to a mechan-

ism that lifts the ground-state degeneracy and spontaneously stabilizes one of the ordered ground states [7]. A prime example is the transformation of a disordered spin glass phase into a chiral vortex phase due to random anisotropy [8, 9]. The leading cause is still not fully understood, argued to be either due to nearest/next nearest neighbor interactions and/or random Dzyaloshiniskii-Moriya interaction (DMI) (Fig. 2.1.1). Chemically and structurally disordered materials have shown to have similar magnetic properties, moments, and states as systems with broken inversion symmetry [11]. The degenerate spin chirality of disordered systems permits isotropic and anisotropic topological spin textures at remanence, differentiating them from systems with global inversion symmetry breaking [11]. Our group also investigates topological spin-textures of materials with a random DMI and order-by-disorder.

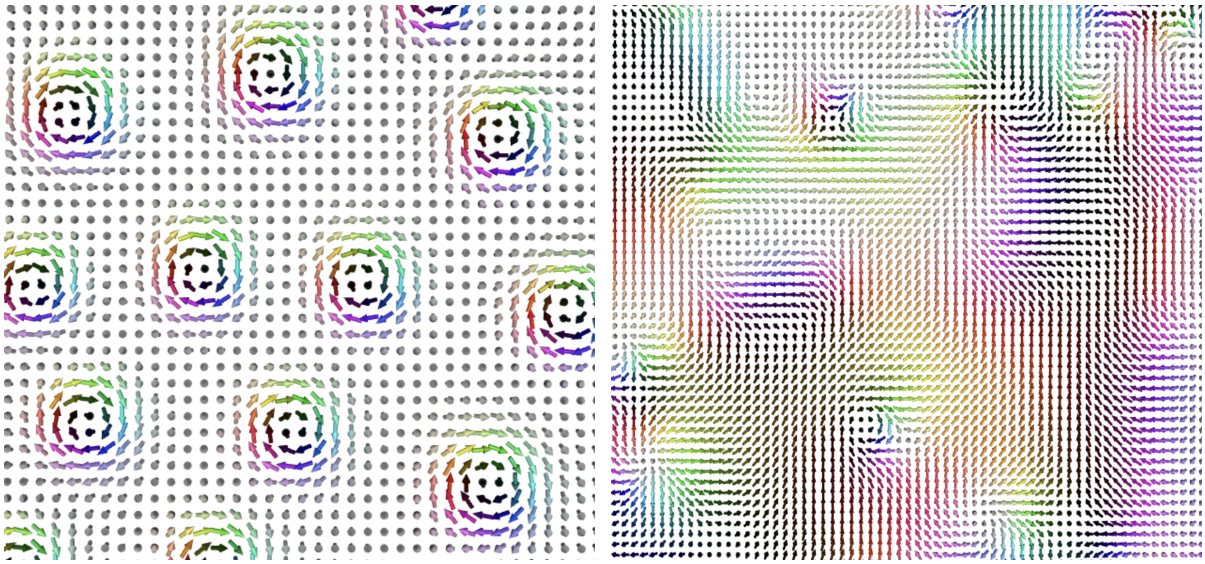

Fig. 2.1.1: *A chiral Bloch skyrmion lattice with DMI is shown in the left. The right illustrates a variety of topological states including Bloch, Neél, and anit-skyrmions generated purely via spin frustration [12].*

2.2 Scope of Thesis

The scope of this thesis is to improve the synthesis of amorphous iron germanium films in terms of structural and magnetic properties, building on our recent work on amorphous thin films with and without nanocrystals [6]. We altered the deposition conditions to obtain soft-magnetic and isotropic disordered films. Comparing the actual composition with the

nominally set composition during deposition reveals different adhesion coefficients that affect film thickness and magnetic properties. The results detail the known structural properties of the films as well as a discussion on the partially known structures of films which require additional measurements to be fully characterized. The variation in coercive fields within and across films is discussed followed by additional magnetic quantities determined from ferromagnetic resonance spectroscopy. The discussion and current conjectures explaining the properties of the films is followed by plans for future measurements to further our investigation and understanding of the films discussed, as well as synthesis of new films.

3 Background

3.1 Introduction

At the end of the nineteenth century the discovery of the electron was a monumental revelation in the field of magnetism [13]. Quantum mechanics and relativity provided an explanation to the source of magnetism at the atomic scale, relating to the angular momentum of elementary particles [14]. Associated with each electron is a magnetic moment, and for unpaired electrons, these moments can either align parallel (adding their magnetic moments) or antiparallel (canceling their magnetic moments) [15, 16]. The determining factor for this alignment is the exchange interaction. Depending on the electronic structure of the material, it is either more energetically favorable for unpaired electrons to be in the singlet or triplet state [15]. If the triplet state is more energetically favorable, the magnetic moments will align parallel. Conversely, if the singlet state is favorable, the moments will align antiparallel, leading to no net magnetic moment. Materials in which the triplet state is favorable are the exception, these materials being characterized as magnetic whereas it is more typical for these moments to cancel with the materials being non-magnetic [15]. However, materials can be excited into the triplet state, exhibiting magnetic behavior. Spin-orbit coupling refers to the relativistic phenomena that occurs between the magnetic field generated by the nucleus in the reference frame of the electron that acts on the electron's magnetic moment [17]. This is dependent on the orbital (L) and spin angular (S) momentum ($AS \cdot L$) of the electron, with the strength of the interaction being proportional to the atomic number (A) [16]. This phenomenon leads to splitting of energy levels of electron orbitals, giving rise to the fine structure, that in turn has the potential to induce or determine a variety of properties that the material possesses, such as magnetic anisotropy and spin relaxation.

3.2 Energy terms

The following description of the free energy and the energy terms comprising it closely follow from the *Magnetic Domain Theory* section of [18].

The magnetization direction within materials is set to minimize the total free energy. The vector field of magnetization directions is given by the unit vector $\vec{m}(r)=\vec{M}(r)/M_S$, with M_S being the saturation magnetization. In conjunction with the constant magnetization constraint (property of atom), the energy minimization implies that the torque on the magnetization must disappear at each point.

Magnetic materials have a free energy that is comprised of a handful of energy terms governed by material properties and interactions. The natural tendency of magnetic materials to minimize this free energy (minimum energy principle) gives rise to what is known as the micromagnetic equations. The calculation of each contributing energy term is dependent on the conditions of the system, leading to complicated, yet all the more interesting, determination of this energy and its role in determining the magnetization direction of the sample and in creating and altering magnetic domains. The micromagnetic equation is derived by minimizing the total free energy made up of the described energy terms:

$$E_{tot} = \int [A(\nabla\vec{m})^2 + F_{an}(\vec{m}) - \vec{H}_{ex}\cdot\vec{M} + \frac{1}{2}\vec{H}_d\cdot\vec{M} - \sigma_{ex}\cdot\epsilon^0 + \frac{1}{2}(p_e-\epsilon^0)\cdot c\cdot(p_e-\epsilon^0)]dV. \quad (3.1)$$

Where the terms following the integral are the exchange, anisotropy, Zeeman, stray field, external stress, and magnetostrictive energy, respectively. Here, F_{an} includes the crystal and structural magnetic anisotropies, σ_{ex} making up the stresses of non-magnetic origin. The free magneto-elastic deformation is given by ϵ^0, the elastic constants tensor is c, and p_e is an asymmetric tensor describing the "actual distortion, the compatible deviation from the initial, 'non-magnetic' state, which will try to approach the free deformation ϵ^0" [18]. All other variables are defined in the discussion below.

The energy terms given in equation 3.1 can be split into local and non-local terms. The local terms given by local magnetization direction values include the anisotropy energy, the Zeeman energy (also known as the applied field energy), the magneto-elastic interaction energy with a stress/strain field of non-magnetic origin [18], and the exchange energy—albeit the calculation method for the exchange energy differs compared to the former three terms. The stray field energy and the magnetostrictive energy comprise the non-local energy

terms. The non-local energy terms lead to the magnetization vector having torques on it that depend at any point on the magnetization directions at every other point [18]. These non-local terms are more complicated to calculate than the local terms, as they cannot be determined by a single integral, requiring two spatial integrations. The stray field and elastic deformations are taken for every given magnetization distribution and integrated to ascertain the minimum energy solely as a function of the magnetization field.

These energy contributions give rise to domains, which are regions within the same sample that are homogeneously magnetized and are dependent on the relative contributions of the different energy terms, the most influential of which being the anisotropy exchange and Heisenberg exchange energy.

3.2.1 Exchange energy

Ferromagnets prefer a consistent stable magnetization direction, and deviations from said direction consequently require energy in return. This energy cost is given by the stiffness expression:

$$E_x = A \int (\nabla \vec{m})^2 dV \tag{3.2}$$

with the exchange stiffness constant A which is dependent on temperature and the material.

With respect to domains, the Heisenberg exchange interaction is one of the most influential energy terms. This interaction occurs between electron spins, indicating that this is a quantum mechanical effect. The exchange energy between electrons can be expressed as [15]

$$E_{ex}^{ij} = -2J\vec{S}_i \cdot \vec{S}_j, \tag{3.3}$$

or for the whole system, considering only nearest neighbor interaction

$$E_{ex}^{ij} = -\sum_{j=1}^{n} J\vec{S}_i \cdot \vec{S}_j \tag{3.4}$$

$\vec{S}_i$ and $\vec{S}_j$ refer to the spins of the electrons and J is exchange constant or exchange integral, which measures the strength and type of interaction. A positive (negative) exchange constant represents ferromagnetic (antiferromagnetic) coupling. The physical origin of the exchange integral is the overlap of the electron orbitals which is represented in the spatial part of the

wave function $\psi_a(r_1)$ and $\psi_b(r_2)$ and the effective Hamiltonian, $\hat{H}$ [15].

$$J = \int \psi_a^*(r_1)\psi_b^*(r_2)\hat{H}\psi_a(r_1)\psi_b(r_2)dr_1dr_2. \tag{3.5}$$

For isotropic and homogenous materials, the exchange constant will be location and orientation independent. A composition gradient will cause a spatial variation of J that can induce a magnetic anisotropy and a preferred magnetic orientation.

3.2.2 Anisotropy

There are multiple types of anisotropy, all of which are extrinsic aside from magnetocrystalline anisotropy. Induced forms include shape, magnetoelastic, and exchange anisotropy [19]. The magnetocrystalline anisotropy energy describes the dependence of the magnetization direction with respect to the crystallographic orientation of the material. This reliance of the magnetization direction relative to the structure of the material arises due to spin-orbit interactions. The anisotropy terms deal with the symmetry of the situation; crystal anisotropies relating to an undisturbed crystal structure and induced anisotropies providing information about straying from symmetry due to, for example, lattice defects and/or partial atomic ordering [18].

3.2.3 Magnetic field energy

The Zeeman energy simply arises from the interaction energy between an external magnetic field (H_{ex}) and the magnetization vector field of the material. It is given by

$$E_H = -M_S \int \vec{H}_{ex} \cdot \vec{m} dV, \tag{3.6}$$

which for a uniform external field, only depends on the average magnetization of the material.

The stray field energy is the second contributor to the magnetic field energy, relating to the magnetic field that the magnetic body generates. The energy related to the stray field ($\vec{H}_d$)

is given by:

$$E_d = -\frac{1}{2}\mu_0 \int_{sample} \vec{H}_d \cdot \vec{M} dV \tag{3.7}$$

and strongly depends on the shape of the material and the magnetic direction with respect to the surface normal.

3.2.4 Magneto-elastic interactions and magnetostriction

The magnetostrictive self-energy is related to the elastic interactions between regions magnetized along different axes. A magnetic body will deform under the influence of a magnetic interaction. This deformation can be described by an asymmetric tensor of elastic distortion, consisting of a symmetric (stress) and an antisymmetric (shear). Strain can be induced in thin films when there is a mismatch between lattices in different layers of the films, such as between the seed layer and magnetic film layer. As film thickness increases, the strain effects relax as the top surface is free of constraints, thus strain effects are more significant in films with thicknesses of a few nanometers. Strain within a thin film can lead to anisotropy as a result of substrate deformation [20].

3.3 Domains

The following discussion on domains and domain walls largely follows from [13].

Domains are regions within a magnetic sample with homogeneous magnetization, that are separated by areas of continuously rotating magnetization (domain walls) and appear when it is more energetically favorable for the magnetization directions to be in different phases to minimize e.g. the stray field energy (Eq. 3.7). The structure of domains is often complicated [18]. Alongside stray field energy, anisotropy energy plays a lead role in domain formation and dynamics. The ratio of anisotropy and stray field energy is known as the quality factor, given by $Q = K/K_d$, where K is the effective anisotropy constant and K_d is the stray field energy coefficient [18]. Hence, if the dominating energy term is the anisotropy, then Q>1 and domains develop around avoiding anisotropy energy penalty whilst attempting to keep the stray field energy to a minimum. Conversely, when the stray field energy term dominates, Q<1, flux-closed domain patterns form to circumvent stray field energy expense

while keeping the anisotropy energy to a minimum (Fig. 3.3.1). The quality factor is utilized as the principal criterion in characterizing domain phenomena as it allows for classifying domains and magnetic materials in a simple manner.

The character and structure of domain walls is dependent on the Q-factor and sample thickness. Additionally, wall angle and magnetostriction can also have influence on structure and character of domain walls. There are two main types of domain walls, Bloch and Néel, which differ in their magnetization rotation across the wall and thus in their energy contributions. Néel walls have a magnetization rotation parallel to the wall plane, having zero stray field energy in bulk regions. Conversely, Bloch walls exhibit a magnetization rotation perpendicular to the wall plane, with maximal stray field energy and negligible surface charges making them favorable in thin films.

Similar to domain phases, anisotropy is also important when it comes to domain walls, the anisotropy energy being roughly proportional to the domain wall energy [3]. The energy of a domain wall consists of anisotropy and exchange energy generated from non-parallel magnetic moments across the wall and magnetization deviating from the anisotropy axes [13]. It is important to note that the rearrangement of domain phases in a magnetic field is responsible for magnetization curves. Generally, the magnetization curves of materials depend on their microstructure or morphology (polycrystalline, amorphous, or nanocrystalline), domain walls being pinned at grain boundaries and/or defects, strain anisotropy, and domains and effective magnetic field. These features are thought to lead to coercivity and irreversibility. Furthermore, domain analysis is often necessary to interpret hysteresis curves and domain response to magnetic fields.

Variations in the magnetization in the form of non-collinear spin textures, such as domain walls, skyrmions, or helical spins, may also occur in materials with higher order exchange interactions even in the absence of demagnetizing effects. This includes competing next-nearest neighbor exchange (spin frustration) and vector exchange (DMI) due to inversion symmetry breaking [13]. The latter is proportional to $\vec{S}_i \times \vec{S}_j$ and hence favors perpendicularly aligned spins opposed to parallel or anti-parallel set by Heisenberg exchange (Eq. 3.3). DMI can lead to homochiral magnetization modulations such as helical spin-spiral phases, the skyrmion topological spin structure (see 2.1.1) being the most prominent. Skyrmions are intrinsically caused magnetic modulations classified as spintextures whereas modulated elements of multidomain states are considered apart of magnetic microstructure.

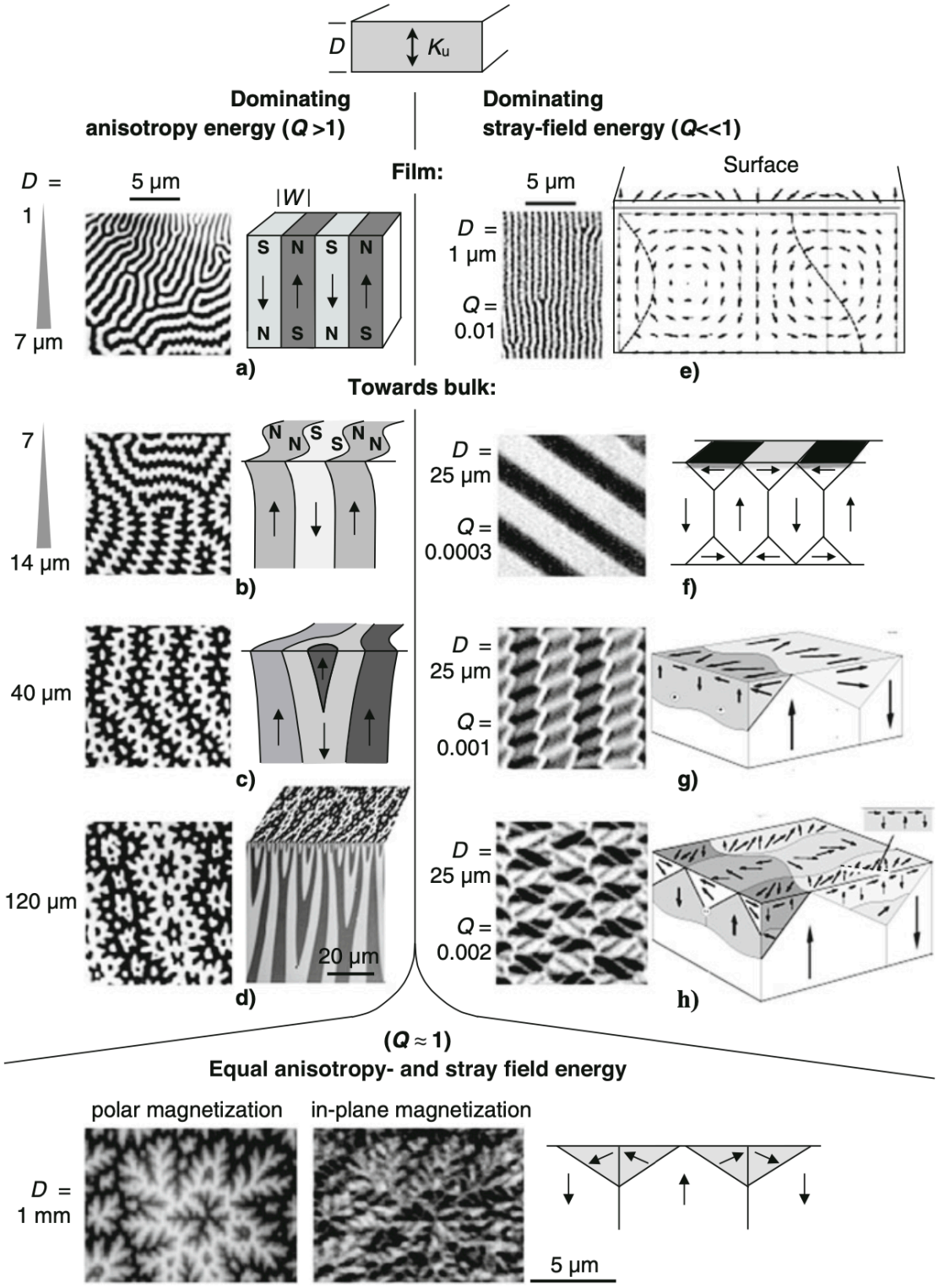

Fig. 3.3.1: *Magnetic domain resulting from variations in relative stray field and anisotropy energy [13].*

3.4 Kerr effect

The magneto-optical Kerr effect (MOKE) leverages polarized light reflected off a magnetic sample that alters the polarization and/or intensity of the reflected light with respect to the incident beam to determine the magnetization of the sample. There are three cases referring to the magnetization direction of the sample: longitudinal, transverse, and polar (see Fig. 3.4.1). For each case, the incident light is linearly polarized, being either p-polarized (in which the light is polarized in the plane made by the incident and reflected light, the incident plane) or s-polarized (perpendicular to the incident plane) [12]. For a magnetized sample, an incident beam of light induces oscillations of the electrons in the sample. If the direction of oscillation of the electrons has a component perpendicular to the direction of magnetization, there will be a Lorentz force ($F = q(E + v \times B)$). A sizable Lorentz force will create a new oscillation component perpendicular to the light polarization plane thereby altering the polarization and/or intensity of the reflected wave [21]. In the longitudinal case, the sample is magnetized in-plane and parallel to the incident plane. For both s and p-polarized incident light, there is a Lorentz force perpendicular to the polarization of the incident light, causing the reflected light to be elliptically polarized and the major axis of the reflected light to be rotated (Kerr rotation) [21]. For transverse MOKE, the sample is magnetized in-plane and perpendicular to the incident plane. For p-polarized light, the Lorentz force causes oscillation in the same direction as the reflected p-polarized light, altering the intensity of the reflected wave but not the polarization. For s-polarized light, the induced oscillations of the electrons in the sample are parallel to the magnetization of the sample, thus there

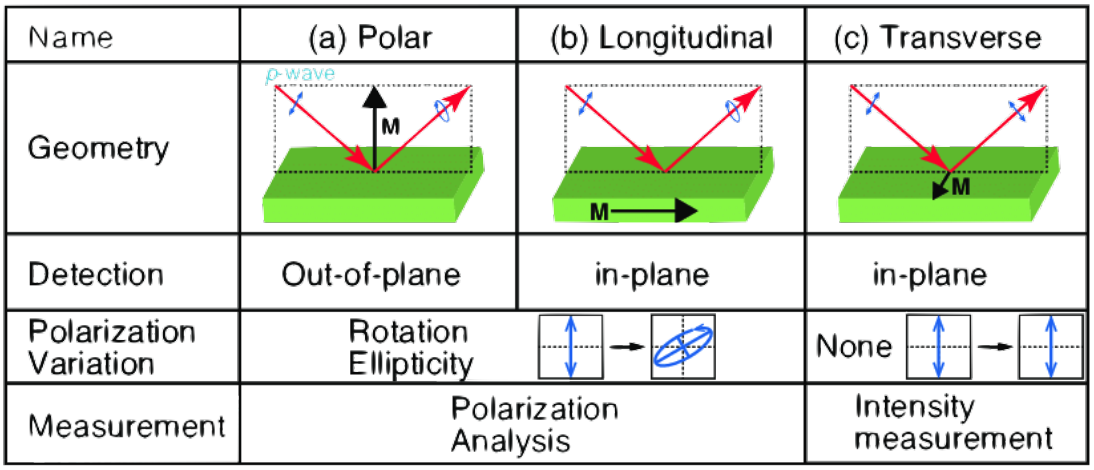

Fig. 3.4.1: *Magneto-optical Kerr effect and its application to measure the magnetization [22].*

is no Lorentz force and consequently the reflected light is unchanged [21]. Lastly, for polar MOKE, the magnetization of the sample is out-of-plane and parallel to the incident plane. For both s and p-polarized light, there is a Lorentz force generated that causes the reflected light to be elliptically polarized with a rotation of the major axis, again proportional to the magnetization. Thus, the magnetization of a sample can be determined by analyzing the polarization of the reflected light for polar and longitudinal magnetization, and by analyzing the intensity of the reflected light for transverse magnetization [21].

3.5 Ferromagnetic resonance

Ferromagnetic resonance (FMR) is a property of magnetic materials that can be leveraged in experiments to ascertain material properties such as saturation magnetization, gyromagnetic ratio, spin damping, inhomogeneous line broadening, and exchange stiffness [23, 24]. When a magnetic material is uniformly magnetized in a set direction, an oscillating magnetic field applied perpendicular to the magnetization can trigger a spin precession about the external field direction. However, dissipative forces (damping) can cause the precession to cease and only driving frequencies near the natural resonance frequency of the magnetization can effectively stimulate a strong precession. The frequency at which the magnetic moment precesses is the Larmour frequency, and hence resonance occurs when the applied AC field is set to the Larmour frequency [24]. By invoking precession of the magnetic moments and measuring magnetization dynamics using broadband FMR spectroscopy, the aforementioned properties can be obtained [23–25].

Determining the magnetic properties of films with FMR is typically done using coplanar waveguide ferromagnetic resonance (CPW-FMR). This entails an external DC magnetic field (H_{DC}) to align the magnetization of the sample while applying an oscillating radio frequency (RF) field to wobble the magnetization of the sample, with the RF signal being carried by the waveguide [25]. The resonance frequency depends on the applied magnetic field; thus, the RF signal can be fixed while sweeping the applied field, producing a resonance spectrum. The Kittel formula can then be used to relate the resonance frequency to the applied field H_{DC} in the form of the power absorption, the saturation magnetization, and the gyromagnetic ratio. Additionally, spin damping and inhomogeneous line broadening can be extracted from the linewidth [23–25].

4 Experimental Methods

4.1 Thin film synthesis

The samples were fabricated using thermal evaporation with a molecular beam epitaxy system (Octoplus 300 MBE Komponenten GmbH). The samples were grown on 300 nm amorphous silicon nitride on silicon (100) wafers (MTI Corporation). The substrates were mounted to copper holders using clamps and placed within the load lock a day prior to the deposition to have sufficient time to degas (10^{-9} mbar). For the deposition, the substrate mounts were positioned on a rotatable manipulator stage housed in the chamber. The materials that are deposited onto the substrate are in effusion cells beneath the substrate, each cell having a shutter programed to open and close after a calculated period based on the deposition rate to achieve the desired film thickness and composition. The iron [United Minerals and Chemicals (UMC), 99.99%] and germanium (UMC, 99.9999%) were co-evaporated, and covered by an aluminum (UMC, 99.9999%) layer. The samples were made in two separate batches, AA64-AA69 being deposited while the manipulator stage remained static and AA70-AA74 being rotated at 20 Hz during the deposition. The iron germanium compositions, aluminum capping layers, thicknesses, and deposition rates were all varied (see table 4.1.1). The aluminum capping layer is used to prevent oxidation of the iron germanium, thus in the first batch I began by testing the desired aluminum thicknesses from 2-5 nm, under the assumption that 5 nm would be more than sufficient to prevent iron germanium oxidation. After creating samples with the same iron germanium compositions and differing capping layer thicknesses, I started to vary the compositions of iron germanium to determine the effects on the magnetic properties. I commenced with values near the $Fe_{50}Ge_{50}$ compositions done for the previous samples, then began with $Fe_{100}Ge_0$ at the start of the second batch, decreasing the iron composition by increments of 10%. The chamber walls were kept cold during sample fabrication using liquid nitrogen yielding a base pressure of 10^{-10} mbar and a vacuum $< 10^{-8}$ mbar during deposition. Due to the radiation heating of the effusion cells, the effective deposition

Sample	Nominal composition	Deposition rate [Å/s] Fe	Ge	Nominal thickness [nm] Fe–Ge	Al
AA64	$Fe_{50}Ge_{50}$	0.15	0.15	40	2
AA65	$Fe_{50}Ge_{50}$	0.15	0.15	40	3
AA66	$Fe_{50}Ge_{50}$	0.15	0.15	40	4
AA67	$Fe_{50}Ge_{50}$	0.15	0.15	40	5
AA68	$Fe_{40}Ge_{60}$	0.10	0.15	40	3
AA69	$Fe_{60}Ge_{40}$	0.15	0.10	40	3
AA70	$Fe_{50}Ge_{50}$	0.15	0.15	40	3
AA71	$Fe_{100}Ge_{0}$	0.15	0.00	30	3
AA72	$Fe_{90}Ge_{10}$	0.15	0.0167	35	3
AA73	$Fe_{80}Ge_{20}$	0.15	0.0375	35	3
AA74	$Fe_{70}Ge_{30}$	0.15	0.0643	35	3

Tab. 4.1.1: *Samples AA64-AA74 and their corresponding nominal composition, deposition rate of iron/germanium, and nominal thicknesses of iron-germanium and aluminum capping layer. Samples AA64-69 remaining static whereas AA70-AA74 were rotated at 20 rpm during deposition.*

temperature for AA64-AA69 and AA70-AA74 measured on the holder was $299 - 317$ K, the actual substrate temperature likely being higher.

4.2 Chemical and structural characterization

The nominal composition and thickness of the films stray from the actual values due to the effects that co-evaporation, deposition rate, and temperature, and the substrate have on the adhesion of the elements being deposited. Energy-dispersive x-ray spectroscopy (EDS) was done using Fe K and Ge K absorption edges to determine the offset from the nominal values given by the evaporation rates on prior samples [6]. Assuming identical atomic radii for Fe (126 pm) and Ge (122 pm) and an iron adhesion of 100%, the relation between the nominal iron germanium film thickness value (t_{set}) and the actual value (t) is given by $t = (x_{set}/x)t_{set}$, where x_{set} is the nominal iron composition that was set during the fabrication process (see table 4.1.1) and x is the actual iron composition determined via EDS (Fe_xGe_{1-x}). The validity of this approximation was confirmed for a previous sample batch using x-ray reflectometry [6]. See chapter 5 for the actual Fe-Ge compositions and thickness. Atomic force microscopy (AFM) was used to characterize the topography of the thin films using a Bruker Dimension Icon AFM with silicon tips on a nitride lever at the Nebraska Center for Materials and

Nanoscience (Lincoln, NE).

4.3 Magnetic characterization

4.3.1 Kerr Microscopy

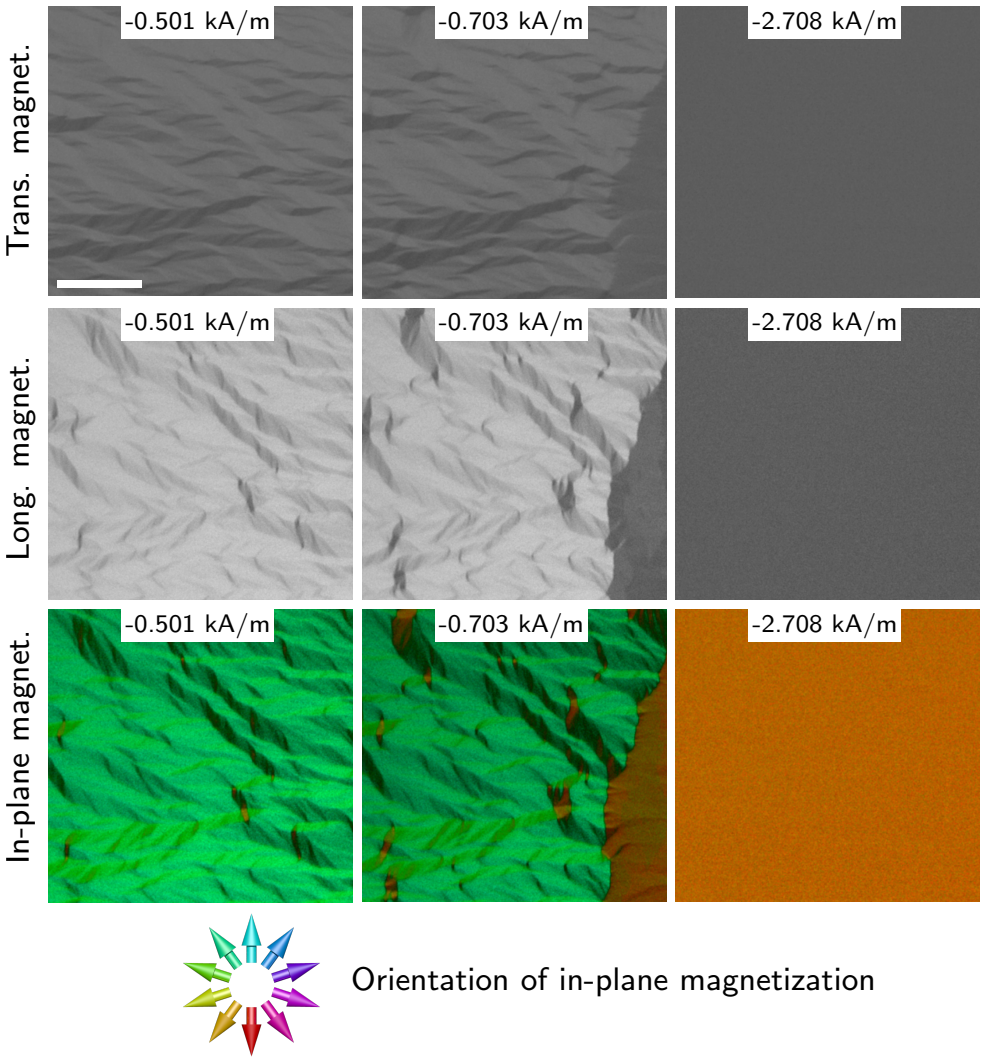

Fig. 4.3.1: *AA70 Kerr microscopy images with transverse, longitudinal, and reconstructed in-plane (bottom row) magnetization at varying magnetic field strength.*

A magneto-optical Kerr effect microscope (EVICO Magnetics) was utilized to record the hysteresis curves (see chapter 5). The microscope enables linearly polarized light to illuminate

the sample in transverse, longitudinal, or polar geometry whilst a varying magnetic field is applied. The in-plane magnet and sample holder are independently rotatable providing means to conduct angle dependent measurements. As the external magnetic field changes through subtracting a DC or AC saturated image, the accompanying domains in the magnetic samples become apparent (Fig. 4.3.1). An xyz piezo stage minimizes thermal drift during measurements. For each sample, a minimum of five areas were measured (the four different edges and the center of the sample, see chapter 5). This was done to examine the homogeneity of the sample in terms of hysteresis curves and domain patterns at the different areas. At roughly the center of each sample, measurements were taken when the sample was rotated 0°, 45°, and 90°. The rotation of the sample while applying the same magnetic field was to survey for anisotropy, whereas measurements in different areas of the same sample investigate potential composition gradients.

4.3.2 Broadband ferromagnetic resonance

FMR broadband spectroscopy was performed inside a DynaCool system (Quantum Design). A coplanar waveguide (250 μm-wide conductor) probing an area of 0.65 mm^2 was used, able to span several of tens of GHz. The microwave signal transmitted by the waveguide does not extend far past the vicinity of the waveguide, hence the samples are placed face-down onto the waveguide to allow for maximum coupling and better excite the spin precession inside the magnetic material. To prevent the waveguide from shorting and scratching, teflon tape was placed between the waveguide and the film [23]. The excitation field frequency was kept fixed using two Helmholtz coils whilst sweeping the DC magnetic bias field to improve sensitivity by lock-in amplification and eliminating frequency dependent background that could potentially mask a weak FMR response [23, 26]. To reduce noise while retaining the width of the resonances, a Savitzky-Golay filter of window length 19 and second-order polynomial was applied to the resulting spectra [26]. As the DC field is swept through the resonance frequency, the magnetization will begin to precess and absorb some of the RF field's energy. The RF field energy is fed into a broadband RF diode that converts it to a voltage [23]. This method allows for distinguishing between intrinsic and extrinsic damping contributions and analyzing the frequency dependence of the resonance linewidth. Not all spectrums can be fitted using a single resonance. Spatial variations in the coercive field, film thickness, anisotropy, and saturation magnetization give rise to a multiplicity of resonances [26]. Each spectrum is fitted by a sum of symmetric and asymmetric Lorentzians derivatives, m, (see Fig. 4.3.2) with the field derivative of the absorption intensity (dP/dH) defined as

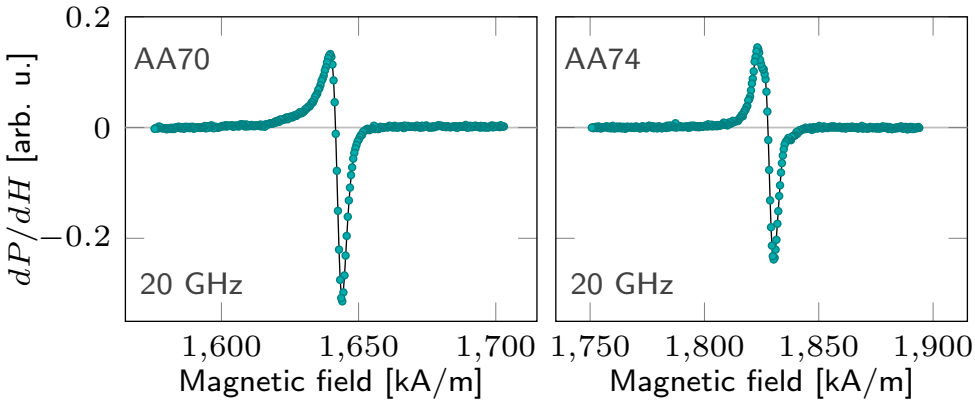

Fig. 4.3.2: *Out-of-plane spectra taken at* 100 *K where AA70 is fitted with a single peak (left) and AA74 with three peaks (right).*

[27]

$$\frac{dP}{dH} = \sum_{i=1}^{m} [a_i \frac{dL_i^{sym}(H)}{dH} + b_i \frac{dL_i^{asym}(H)}{dH}], \tag{4.1}$$

$$L_i^{sym}(H) = \frac{(\frac{1}{2}\Delta H_i)^2}{(\frac{1}{2}\Delta H_i)^2 + (H - H_{res}^i)^2}, \tag{4.2}$$

$$L_i^{asym}(H) = L_i^{sym}(H) \cdot \frac{H - H_{res}^i}{\frac{1}{2}\Delta H_i}. \tag{4.3}$$

Here, H is the bias field, H_{res}^i are the resonance fields, full widths at half maximum (FWHM) given by ΔH_i, and a_i and b_i express the mixing of symmetric to asymmetric Lorentzians. The coefficients a_i and b_i identify contributions of the spectrum composed of different regions that possess varying structural and magnetic properties. Using this method, the resonance fields, intensities, and FWHM can be determined simultaneously [26]. The relationship between resonance field and frequency can be quantified using Kittel's equations for in-plane ($f_{res}^{\parallel}$) and out-of-plane ($f_{res}^{\perp}$) geometry. By those means, the saturation magnetization M_S, the gyromagnetic ratio $\gamma = g\mu_B/\hbar$, μ_B referring to the Bohr magneton, as well as the isotropic in-plane ($H_{\parallel}$) and magnetic anisotropic out-of-plane ($H_{\perp}$) fields are ascertained. Their anisotropies can be related by $K = \frac{1}{2}\mu_0 M_s H$. The in-plane Kittel equation is given by [24, 28]

$$2\pi f_{res}^{\parallel} = \gamma\mu_0 \sqrt{(H_{res}^{\parallel} + H_{\parallel})(H_{res}^{\parallel} + H_{\parallel} - H_{\perp} + M_S)} \tag{4.4}$$

and the corresponding out-of-plane equation by [24, 28]:

$$2\pi f_{res}^{\perp} = \gamma\mu_0(H_{res}^{\perp} - H_{\perp} - M_S). \tag{4.5}$$

Here, $H_{\perp}$ refers to a normal easy-axis (positive) and easy-plane anisotropy (negative). From the FWHM linewidth of the resonance (main resonance in cases where $m > 1$) the Gilbert spin damping constant α, inhomogeneous line broadening ΔH_0, and the frequency and temperature dependence of the quality factor $Q = H_{res}/\Delta H$ [29] can be determined [30]:

$$\Delta H = \Delta H_0 + \frac{4\pi\alpha f}{\gamma} + \Delta H_{\Gamma} \tag{4.6}$$

The term ΔH_{Γ} describes the line broadening of uniform spin precession modes attributable to two-magnon scattering [31–35] on defects [36–38] for in-plane resonances and induces a strong non-linearity with the excitation frequency.

5 Results and Analysis

5.1 Structure

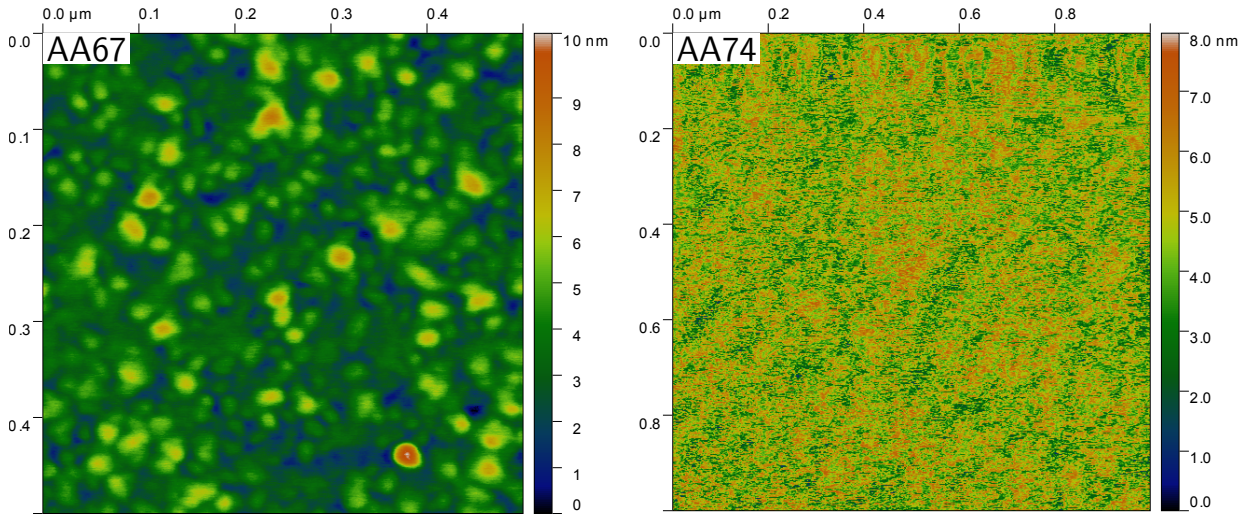

Fig. 5.1.1: *Atomic force microscopy images for AA67 ($Fe_{62}Ge_{38}$) alongside AA74 ($Fe_{83}Ge_{17}$).*

The nanogranularity with a surface roughness of 1.1 nm observed with AFM in AA67 ($Fe_{62}Ge_{38}$) is either due to crystalline nanograins in the film or to particle agglomerations that grew in size during deposition. Considering similar deposition conditions for AA64-AA66 and AA68-AA69, these samples are assumed to have similar structural properties, also conceivably possessing crystalline nanograins and/or have the previously described particle agglomeration growth during synthesis. Films AA70-AA74 were homogeneous with no signs of nanogranularity and a surface roughness ranging from 0.6 nm to 1.2 nm (see Fig. 5.1.1). Samples have yet to be confirmed to be amorphous via XRD. The actual film composition retrieved from EDS, along with the calculated iron-germanium thickness, aluminum capping thickness, and iron/germanium deposition rate are listed in table 5.1.1. The error for the iron composition determined via EDS ranged from $4-6\%$ for AA64-AA69 and from $8-16\%$

Sample	Composition	Deposition rate [Å/s]		Thickness [nm]	
		Fe	Ge	Fe–Ge	Al
AA64	$Fe_{62}Ge_{38}$	0.15	0.15	32.26	2
AA65	$Fe_{62}Ge_{38}$	0.15	0.15	32.26	3
AA66	$Fe_{60}Ge_{40}$	0.15	0.15	33.33	4
AA67	$Fe_{62}Ge_{38}$	0.15	0.15	32.26	5
AA68	$Fe_{50}Ge_{50}$	0.10	0.15	30.00	3
AA69	$Fe_{72}Ge_{28}$	0.15	0.10	33.33	3
AA70	$Fe_{57}Ge_{43}$	0.15	0.15	35.09	3
AA71	$Fe_{100}Ge_{0}$	0.15	0.00	30.00	3
AA72	$Fe_{90}Ge_{10}$	0.15	0.0167	35.00	3
AA73	$Fe_{86}Ge_{14}$	0.15	0.0375	32.56	3
AA74	$Fe_{83}Ge_{17}$	0.15	0.0643	29.52	3

Tab. 5.1.1: *Samples AA64-AA69 (static during deposition) and AA70-AA74 (rotated during deposition) and their corresponding composition determined via EDS, deposition rate of iron/germanium, and thickness of iron-germanium (calculated) and aluminum capping layer (nominal).*

for AA70-AA74. The calculated film thickness agrees well with the expected value derived from x-ray reflectometry on AA67 ($Fe_{62}Ge_{38}$) and highlights the distinct adhesion coefficients for iron and germanium.

5.2 Magnetic properties arising from composition gradient

The spatial variations in coercive field observed in samples AA64-AA69 are likely caused by an iron germanium composition gradient as a result of remaining static during deposition [Fig. 5.2.1(a)]. Considering the cells housing iron and germanium are not directly beneath the center of the stage holding the substrates during deposition, it is feasible that the iron and germanium particles were inhomogeneously distributed across the substrate. Conversely, the coercivity measured at different locations on AA70-AA74 is roughly equal [see Fig. 5.2.2(a)], further implying a composition gradient for the AA64-AA69 batch that can be avoided by rotation during deposition.

The angular dependence of the in-plane coercive field in Fig. 5.2.1(b) is shown for 0°, 45° and 90° revealing apparent easy and hard axes behavior for AA66 ($Fe_{60}Ge_{40}$) and AA67 ($Fe_{62}Ge_{38}$). The in-plane anisotropy is likely strain induced by the composition gradient.

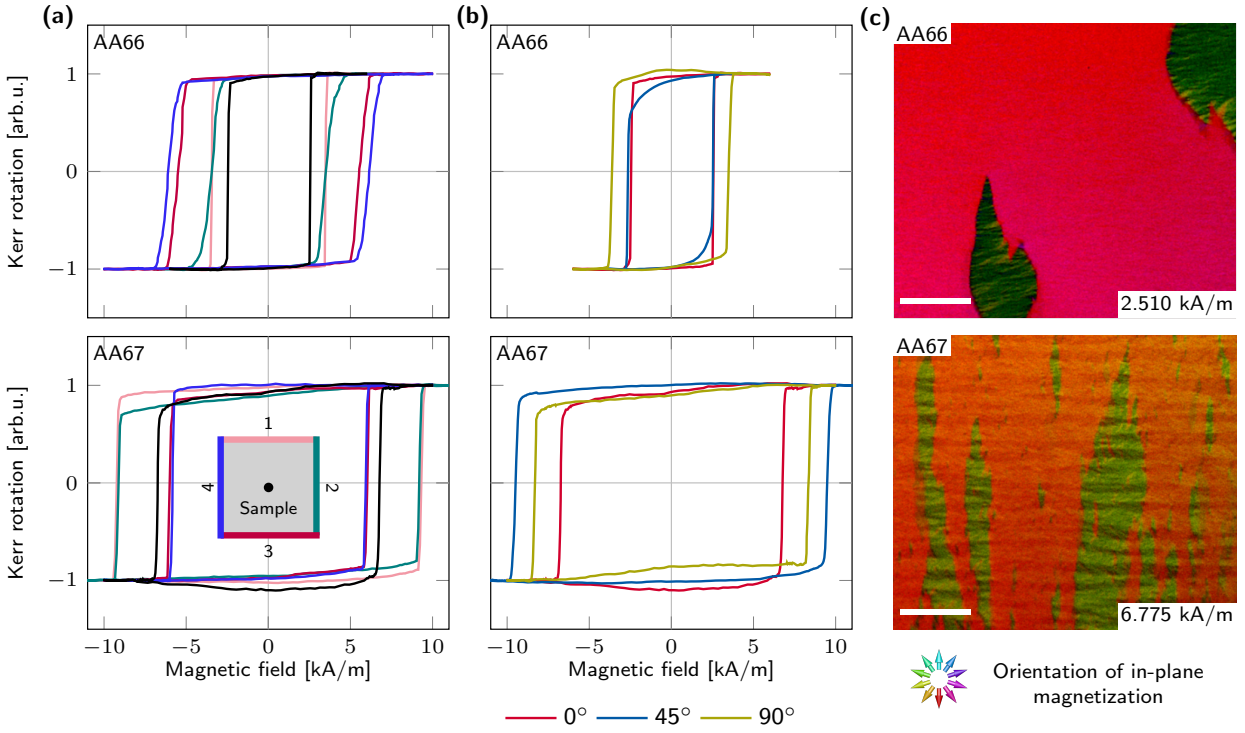

Fig. 5.2.1: *Kerr microscopy hysteresis curves for AA66 ($Fe_{60}Ge_{40}$) and AA67 ($Fe_{62}Ge_{38}$) at different spatial locations, (a), taken at each edge location and at the center (corresponding to black hysteresis loops) as shown in the sample diagram in (a). In (b), measurements were taken at the center with the sample rotated 0°, 45°, and 90°. The reconstructed in-plane magnetization images for AA66 and AA67 are seen in (c) with a 25 μm scale bar.*

This is in contrast to sample batch AA70-AA74 [Fig. 5.2.1(b)], that shows no preferential magnetization axis. From analyzing the hysteresis loops measured with a Kerr microscope, AA64-AA69 appear to be mostly hard-magnetic. Films AA70-AA74 were mixed with AA70 ($Fe_{57}Ge_{43}$), AA72 ($Fe_{90}Ge_{10}$), and AA74 ($Fe_{83}Ge_{17}$) being soft-magnetic whereas AA71 ($Fe_{100}Ge_0$) and AA73 ($Fe_{86}Ge_{14}$) are hard-magnetic. However, AA71 ($Fe_{100}Ge_0$) and AA73 ($Fe_{86}Ge_{14}$) were significantly softer than AA64-AA68 on average.

Broadband FMR spectroscopy was performed on AA70 ($Fe_{57}Ge_{43}$), AA71 ($Fe_{100}Ge_0$), and AA74 ($Fe_{83}Ge_{17}$), see Fig. 5.2.3 and 5.2.4. These samples have mixed results for temperature dependence of the saturation magnetization. For AA70 ($Fe_{57}Ge_{43}$) and AA74 ($Fe_{83}Ge_{17}$), the saturation magnetization decreased with increasing temperature whereas saturation magnetization was roughly static with change in temperature for AA71 ($Fe_{100}Ge_0$). The samples have negligible in-plane anisotropy (<1 kA/m) and a more pronounced perpendicular anisotropy, however for AA71 ($Fe_{100}Ge_0$) and AA74 ($Fe_{83}Ge_{17}$), perpendicular anisotropy falls

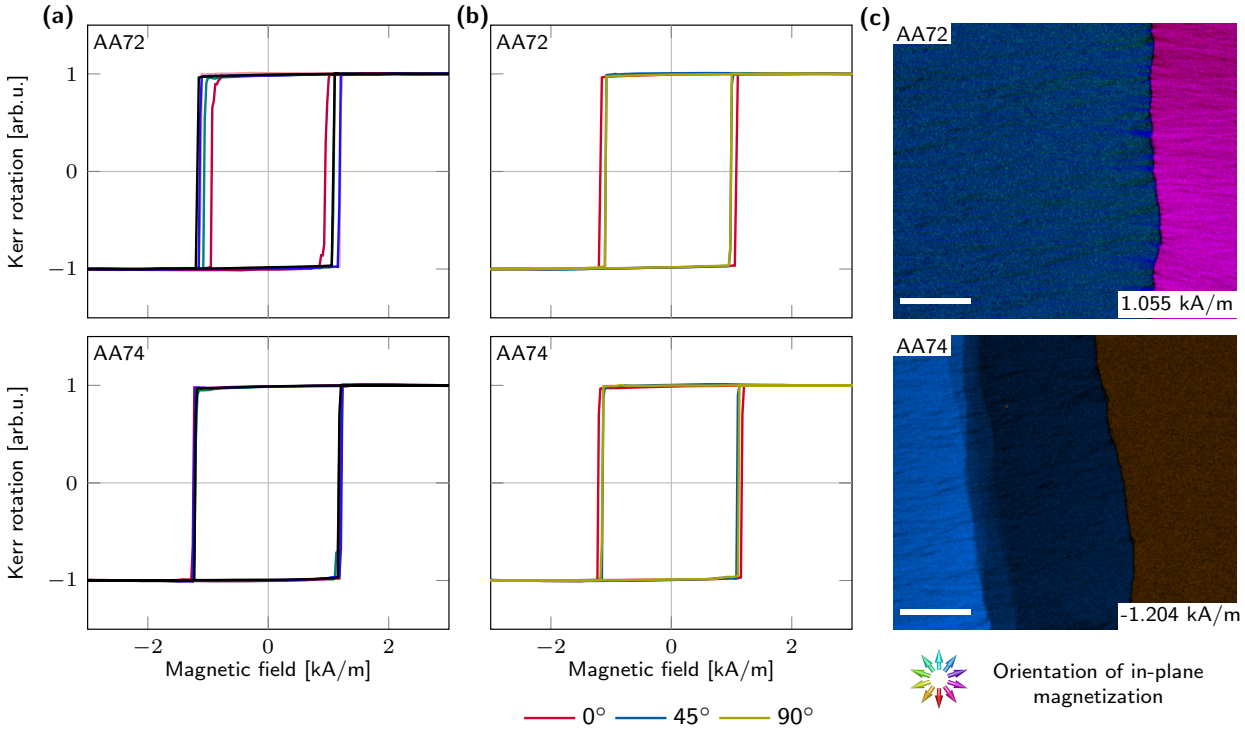

Fig. 5.2.2: *Kerr microscopy hysteresis curves for AA72 ($Fe_{90}Ge_{10}$) and AA74 ($Fe_{83}Ge_{17}$) at different spatial locations (a) taken at each edge location and at the center (corresponding to black hysteresis loops) as shown in the sample diagram in Fig. 5.2.1(a). In (b), measurements were taken at the center with the sample rotated 0°, 45°, and 90°. The reconstructed in-plane magnetization images for AA72 and AA74 are seen in (c) with a 25 μm scale bar.*

within negligible values when considering margin of error (Tab. 5.2.1). The in-plane ($g_{\parallel}$) and out-of-plane ($g_{\perp}$) Landé factors can be found in table 5.2.1. Values of g for pure iron are $g = 2.085$ [39, 40], thus deviating somewhat significantly from these values. Samples AA70 ($Fe_{57}Ge_{43}$) and AA74 ($Fe_{83}Ge_{17}$) were lower consistently for both in-plane and out-of-plane, potentially due to the germanium interacting with the iron to minimize these values and deviating from the value for pure iron. However, AA71 ($Fe_{100}Ge_{0}$) is expected to match literature values, requiring further investigation. The quality factor ranged from 1-32 for in-plane, increasing with increasing frequency, and 150-455 for out-of-plane, decreasing with increasing frequency (Fig. 5.2.5).

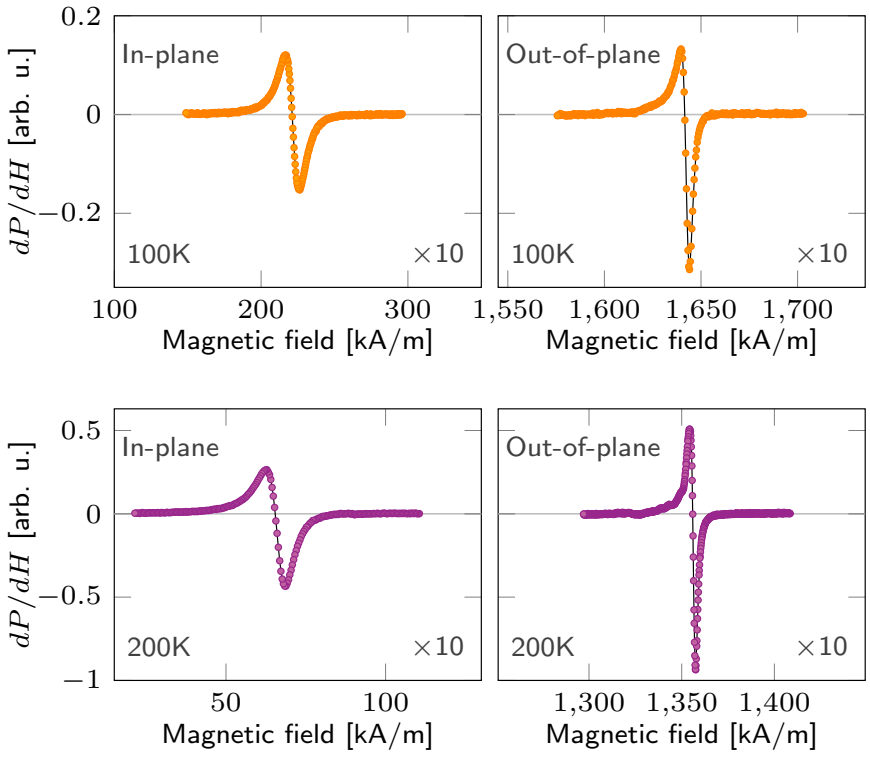

Fig. 5.2.3: *In-plane and out-of-plane spectra taken at 100 K and 200 K for sample AA70 ($Fe_{57}Ge_{43}$).*

Sample	$g_{\parallel}$	$g_{\perp}$	M_S (kA/m)	$K_{\parallel}$ (kA/m)	$K_{\perp}$ (kA/m)
AA70	2.082±0.003	2.067±0.004	1038±3	0.326±0.066	−6.386 ± 1.904
AA71	2.141±0.056	2.056±0.005	1537±52	0.000±0.676	45.469±51.637
AA74	2.008±0.010.	2.046±0.005	1241±11	0.234±0.236	−4.132 ± 8.850

Tab. 5.2.1: *Extracted ferromagnetic resonance broadband spectroscopy values, including in-plane and out-of-plane Landé factor, saturation magnetization, and in-plane and out-of-plane anisotropy field.*

5.3 Domains

Domain patterns visualized with Kerr microscope varied significantly between AA64-AA69 and AA70-AA74. Generally, domains for AA64-AA69 were smaller and took a greater range of external field values to sweep through before becoming saturated, appearing to have some defects where switching required higher fields, relative to the strength of the field required to switch the majority of the film, to align with the external field. Conversely, AA70-AA74 re-

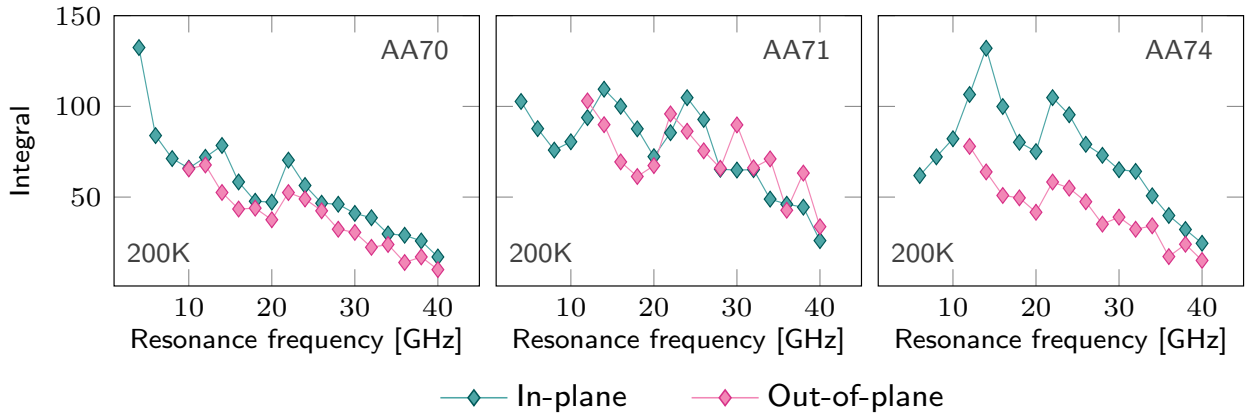

Fig. 5.2.4: *In-plane and out-of-plane integral for samples AA70 ($Fe_{57}Ge_{43}$), AA71 ($Fe_{100}Ge_0$), and AA74 ($Fe_{83}Ge_{17}$) at 200 K.*

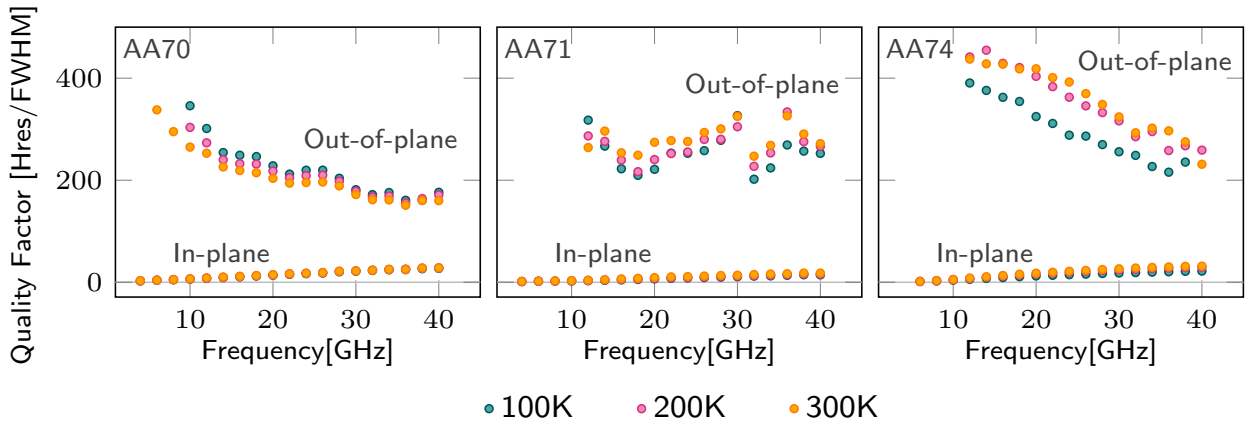

Fig. 5.2.5: *In-plane and out-of-plane quality factor for samples AA70 ($Fe_{57}Ge_{43}$), AA71 ($Fe_{100}Ge_0$), and AA74 ($Fe_{83}Ge_{17}$) at various temperatures taken at 2 GHz.*

quired a notably smaller range of external field values before becoming fully saturated. While the samples had a range of relative domain sizes, compared to AA64-AA69, the domains reconstructed with Kerr microscopy for AA70-AA74 were large [see Fig. 5.2.1(c) and 5.2.2(c)], with occasional smaller domains seen before large-domain switching or after large domains had switched. The smaller domains in AA70-AA74 were larger than domains characteristic of the AA64-AA69 films and likely caused by defects and/or local variations in magnetic anisotropy, exchange and saturation magnetization.

5.4 Conclusion

The two batches with and without sample rotation during deposition exhibit distinct structural and magnetic properties. The uniform samples AA70-AA74 show no signs of nanogranularity (Fig. 5.1.1) and are soft-magnetic with large domains and on average homogeneous (Fig. 5.2.2). Films AA64-AA69 are hard-magnetic with small domains and a spatial and angular dependence of the in-plane coercive field (Fig. 5.2.1). The spatial differences most likely arise from an iron germanium composition gradient created during deposition, and the in-plane anisotropy seen from the angle dependent coercive fields likely strain induced due to the suggested iron germanium composition gradient. Experimental corroboration of this conclusion is ongoing. The differences between the two batches suggest that this potential gradient can be prevented through rotating substrates during the deposition process. The negligible in-plane anisotropy was confirmed by FMR spectroscopy in samples AA70 ($Fe_{57}Ge_{43}$), AA71 ($Fe_{100}Ge_{0}$), and AA74 ($Fe_{83}Ge_{17}$). The gyromagnetic ratios from FMR spectroscopy require further investigation for adequate explanation.

6 Outlook

Additional measurements are needed to further characterize the structure and magnetic properties of the thin films. This includes performing AFM on samples AA64-AA66 and AA68-AA69 to confirm their (dis)similarity in structure to AA67 and XRD to determine whether the samples are (non-)crystalline. Comparing the Landé factor derived from ferromagnetic resonances with the orbital-to-spin moment ratio obtained with X-ray magnetic circular dichroism spectroscopy will help disambiguate the electron orbital hybridization. Recording the transverse and longitudinal conductivity at different temperatures can provide means to correlate structural, magnetic, and electronic transport properties. As the structure and magnetic properties of the films have shown to be extremely sensitive to deposition conditions, other deposition conditions will be systematically altered to better understand the effects of each on the resulting samples. This includes using alternate mounts, using silver paint to adhere substrates to mounts opposed to clamps, and changing the substrate holder (copper, tantalum) to study the effect of radiation heating from effusion cells. To attempt to lower the saturation magnetization measured in samples AA70-AA71 and AA74, future sample batches will have increasing compositions of germanium, with the objective of creating iron germanium films capable of stabilizing topological phases.

Bibliography

[1] C. Lacroix, P. Mendels, and F. Mila, *Introduction to Frustrated Magnetism: Materials, Experiments, Theory* (Springer Berlin Heidelberg, 2011).

[2] P. Nordblad, in *Encyclopedia of Condensed Matter Physics*, edited by F. Bassani, G. L. Liedl, and P. Wyder (Elsevier, Oxford, 2005) pp. 452–457.

[3] A. Zaccone, *Theory of Disordered Solids: From Atomisitic Dynamics to Mechanical, Vibrational, and Thermal Properties* (Springer International Publishing, 2023).

[4] K.-H. Dahmen, *Encyclopedia of Physical Science and Technology*, third edition ed., edited by R. Meyers (Academy Press, 2003).

[5] M. Ohring, *Materials sciences of thin films* (Academic Press, 2001).

[6] R. Zielinski, N. Nguyen, B. Herrington, A. Tarkian, O. Taha, W. K. Chin, A. Mahmood, X. Chen, C. Klewe, P. Shafer, J. Ciston, P. Ashby, C. Mazzoli, and R. Streubel, *Magnetic order in nanogranular iron germanium ($Fe_{0.53}Ge_{0.47}$) films.* J. Phys.: Condens. Matter **37**, 045802 (2025).

[7] A. Hickey, D. Lozano-Gómez, and M. J. P. Gingras, *Order-by-disorder without quantum zero-point fluctuations in the pyrochlore heisenberg ferromagnet with dzyaloshinskii-moriya interactions* (2025), arXiv:2403.02391 [cond-mat.str-el] .

[8] J. Villain, J. P. Bidaux, R. Carton, and R. Conte, *Ordering due to disorder in dipolar magnets on two-dimensional lattices.* J. Phys. (Paris) **41**, 1263 (1980).

[9] R. Streubel, N. Kent, S. Dhuey, A. Scholl, S. Kevan, and P. Fischer, *Spatial and temporal correlations of XY macro spins.* Nano Lett. **18**, 7428 (2018).

[10] *How to harness local inversion symmetry breaking for 3d nano magnetism?*

[11] R. Streubel, D. S. Bouma, F. Bruni, X. Chen, P. Ercius, J. Ciston, A. T. N'Diaye, S. Roy, S. Kevan, P. Fischer, and F. Hellman, *Chiral spin textures in amorphous iron-germanium thick films*. Adv. Mater. **33**, 2004830 (2021).

[12] G. P. Müller, M. Hoffmann, C. Dißelkamp, D. Schürhoff, S. Mavros, M. Sallermann, N. S. Kiselev, H. Jónsson, and S. Blügel, *Spirit: Multifunctional framework for atomistic spin simulations*. Phys. Rev. B **99**, 224414 (2019).

[13] S. S. P. Parkin and J. M. D. Coey, *Handbook of Magnetism and Magnetic Materials*, 1st ed. (Springer International Publishing, Cham, 2021).

[14] S. Tomonaga, *The story of spin* (University of Chicago Press, Chicago, 1997).

[15] C. Kittel, *Introduction to Solid State Physics*, eighth edition ed. (Wiley, 2005).

[16] S. Blundell, *Magnetism in Condensed Matter* (Oxford University Press, 2001).

[17] S. Majumdar, H. Majumdar, R. Österbacka, and E. McCarthy, in *Reference Module in Materials Science and Materials Engineering* (Elsevier, 2016).

[18] A. Hubert and R. Schäfer, *Magnetic Domains* (Springer, 1998).

[19] *What is magnetic anisotropy?*

[20] T. Thomson, in *Metallic Films for Electronic, Optical and Magnetic Applications*, edited by K. Barmak and K. Coffey (Woodhead Publishing, 2014) pp. 454–546.

[21] J. Hall, *Magneto-optic kerr effect (moke)* (2021).

[22] S. Yamamoto and I. Matsuda, *Measurement of the resonant magneto-optical kerr effect using a free electron laser*. Applied Sciences **7** (2017), 10.3390/app7070662.

[23] *Introduction to: Broadband fmr spectroscopy*.

[24] C. Kittel, *Ferromagnetic resonance*. Journal de Physique et le Radium (1951).

[25] O. Yalcin, *Ferromagnetic resonance: Theory and applications* (IntechOpen, 2013).

[26] N. Nguyen, B. Herrington, K. Chorazewicz, S.-F. P. Wang, R. Zielinski, J. Turner, P. D. Ashby, U. Kilic, E. Schubert, S. Mathias, R. A. Parrott, A. A. Sweet, and R. Streubel, *Ferromagnetic resonators synthesized by metal-organic decomposition epitaxy.* J. Phys.: Condens. Matter **35**, 485801 (2023).

[27] L. Liu, T. Moriyama, D. C. Ralph, and R. A. Buhrman, *Spin-torque ferromagnetic resonance induced by the spin hall effect.* Phys. Rev. Lett. **106**, 036601 (2011).

[28] M. Farle, *Ferromagnetic resonance of ultrathin metallic layers.* Rep. Prog. Phys. **61**, 755 (1998).

[29] I. W. Selesnick, *Wavelet transform with tunable q-factor.* IEEE Trans. Signal Process. **59**, 3560 (2011).

[30] E. I. Green, *The story of q.* American Scientist **43**, 584 (1955).

[31] J. Lindner, K. Lenz, E. Kosubek, K. Baberschke, D. Spoddig, R. Meckenstock, J. Pelzl, Z. Frait, and D. L. Mills, *Non-gilbert-type damping of the magnetic relaxation in ultrathin ferromagnets: Importance of magnon-magnon scattering.* Phys. Rev. B **68**, 060102 (2003).

[32] G. Woltersdorf and B. Heinrich, *Two-magnon scattering in a self-assembled nanoscale network of misfit dislocations.* Phys. Rev. B **69**, 184417 (2004).

[33] R. McMichael and P. Krivosik, *Classical model of extrinsic ferromagnetic resonance linewidth in ultrathin films.* IEEE Trans. Magn. **40**, 2 (2004).

[34] K. Lenz, H. Wende, W. Kuch, K. Baberschke, K. Nagy, and A. Jánossy, *Two-magnon scattering and viscous gilbert damping in ultrathin ferromagnets.* Phys. Rev. B **73**, 144424 (2006).

[35] S. Emori, U. S. Alaan, M. T. Gray, V. Sluka, Y. Chen, A. D. Kent, and Y. Suzuki, *Spin transport and dynamics in all-oxide perovskite $La_{2/3}Sr_{1/3}MnO_3/SrRuO_3$ bilayers probed by ferromagnetic resonance.* Phys. Rev. B **94**, 224423 (2016).

[36] R. Arias and D. L. Mills, *Extrinsic contributions to the ferromagnetic resonance response of ultrathin films.* Phys. Rev. B **60**, 7395 (1999).

[37] R. Arias and D. L. Mills, *Extrinsic contributions to the ferromagnetic resonance response of ultrathin films*. J. Appl. Phys. **87**, 5455 (2000).

[38] R. D. McMichael, D. J. Twisselmann, and A. Kunz, *Localized ferromagnetic resonance in inhomogeneous thin films*. Phys. Rev. Lett. **90**, 227601 (2003).

[39] J. M. Shaw, R. Knut, A. Armstrong, S. Bhandary, Y. Kvashnin, D. Thonig, E. K. Delczeg-Czirjak, O. Karis, T. J. Silva, E. Weschke, H. T. Nembach, O. Eriksson, and D. A. Arena, *Quantifying spin-mixed states in ferromagnets*. Phys. Rev. Lett. **127**, 207201 (2021).

[40] C. T. Chen, Y. U. Idzerda, H.-J. Lin, N. V. Smith, G. Meigs, E. Chaban, G. H. Ho, E. Pellegrin, and F. Sette, *Experimental confirmation of the x-ray magnetic circular dichroism sum rules for iron and cobalt*. Phys. Rev. Lett. **75**, 152 (1995).

Acknowledgements

During my time working on my thesis, many people provided great assistance, without whom I would not have been able to achieve success. I would like to acknowledge each in the following.

Dr. Streubel (Department of Physics and Astronomy) for allowing me to be apart of the Streubel Lab during my undergraduate studies and who took significant time out of his schedule to provide crucial feedback on constructing and editing my thesis.

Dr. Adenwalla (Department of Physics and Astronomy) for having fruitful conversations as well as giving great insight and invaluable assistance in editing my thesis.

Omar Taha (Department of Physics and Astronomy) for his contributions in the structural characterization, including AFM, EDS, and XRR measurements.

Nhat Nguyen (Department of Physics and Astronomy) for his assistance with previous work that my thesis builds upon. Additionally, for continued interesting discussions relating to material sciences.

Bryce Herrington (Department of Physics and Astronomy) for helpful conversations throughout our studies together that aided my comprehensive understanding of the topics discussed in my thesis.